PAPER

Check for updates

K+ selectivity modulation in non-aqueous CO_2 electroreduction on lead catalysts: from oxalic to tartaric acid production†

Eduardo Arizono dos Reis, [iD] ab Gelson T. S. T. da Silva [iD] c and Caue Ribeiro [iD] *abc

Here, we show that the presence of potassium ions in the catholyte modulates the selectivity of a Pb plate electrode, leading to the formation of tartrate, a C_4 compound, from CO_2 reduction. A faradaic efficiency of 60% was achieved at -2.3 V (*vs.* Ag/Ag+) for tartrate using a proton exchange membrane and a high concentration of potassium-based supporting anolyte. The electrode microenvironment with a higher potassium concentration also inhibits cathode corrosion and deactivation. Remarkably, the electroreduction of CO_2 changes the selectivity with the cationic availability in the anolyte. Higher FE to formic acid is observed with an increase in the proton concentration, and by increasing anolyte K+ availability, C–C coupled products (oxalate, C_2, and tartrate, C_4) are formed in the majority. Our results prove that controlling potassium ions and the proton concentration in the catholyte regulates the selectivity of the Pb plate electrode and can lead to the formation of a C_{2+} product from CO_2 reduction.

1. Introduction

Implementing carbon-capture technology for CO_2 directly from industrial waste gases can overcome the low benchmark atmosphere capture cost[1,2] and use high purity CO_2 emission to convert carbon dioxide into other molecules of industrial chemical interest.[3–7] Among the various techniques for dioxide conversion, the electrochemical CO_2 reduction reaction (CO_2RR) is a growing approach[8–10] due to the multiple pathways capable of producing all the top globally consumed carbonaceous products[11] using a flexible suite of electricity-mediated reduction that can tune the selectivity of the value-added products obtained.[8,11] One of the limitations of the CO_2RR in aqueous media is driving the high-energy steps for activating CO_2 reduction at a moderate potential for a specific product.[12,13] Due to the high inertness of CO_2 molecules associated with their low solubility in aqueous electrolytes (33 mM at 1 atm and 25 °C), the hydrogen evolution reaction (HER) is the main issue for achieving high current efficiencies.[14] An effective way to circumvent the high reaction rates and suppress the HER is by engineering the reaction environment. Several strategies, such as ionic liquid electrolytes, gas phase reactions, and aprotic

solvents, have been used.[15–19] In the CO_2RR, aprotic solvents can give more complex C_{2+} molecules as products (oxalic acid, glycolic acid, and glyoxylic acid), leading to new CO_2-based polymers.[20] Among the few electrocatalysts reported in the literature, lead-based electrodes are the most efficient catalyst to convert CO_2 into C_{2+} products with higher faradaic efficiency,[15,16,21–28] but their selectivity relies mainly on the electrolyte solvent[19,22,29] and proton availability.[22,30–32]

Using the non-aqueous electrolyte in a GDE flow cell configuration is far from an actual application.[3,21] More basic studies are still necessary since old previous publications lack sufficient analysis, report misleading analytical data, and present conflicting reactivity.[21,33] At the same time, microenvironment modulation has been found to be a critical factor in electrochemical reactions rather than just investigating new catalysts.[34,35] The electrocatalyst microenvironment can play an essential role in the activity and selectivity of the reaction either by increasing the reactant at the interface or/and by the stabilization of the intermediates close to the electrode surface, favouring the formation of multielectron reduction products.[36–40] In non-protic organic media, electrolyte ions, metal centre catalysts, solvent, and water content are the primary investigated interfacial microenvironment regulators for the CO_2RR.[19,22,32,41,42] Recently, high concentrations of local alkali ions have been demonstrated to inhibit proton diffusion and favour carbon–carbon (C–C) coupling reactions in aqueous electrolytes.[43–47] Understanding the significance of alkali ions present in the electrolyte, regarding the solubility limit, and the ion migration effect on the selectivity of the CO_2 reduction reaction is an unexplored field for non-protic electrolytes.

aSão Carlos Institute of Chemistry, University of São Paulo (USP), São Carlos, São Paulo, Brazil

bNanotechnology National Laboratory for Agriculture (LNNA), Embrapa Instrumentation, São Carlos, São Paulo, Brazil. E-mail: caue.ribeiro@embrapa.com.br

cDepartment of Chemistry, Interdisciplinary Laboratory of Electrochemistry and Ceramics, Federal University of São Carlos, São Carlos, São Paulo, Brazil

† Electronic supplementary information (ESI) available. See DOI: https://doi.org/10.1039/d4ta01172d

This journal is © The Royal Society of Chemistry 2024

J. Mater. Chem. A, 2024, 12, 15829–15836 | 15829

In this sense, we propose an unprecedented strategy to promote C_{2+} product formation in non-aqueous CO_2RR, using a cation exchange membrane to regulate the reaction by the cation migration effect on flat Pb plate cathodes and tuning product selectivity by anolyte selection. We used electro-chemical measurements to demonstrate that the anolyte pH influences the CO_2 reduction activity and selectivity. Additionally, this work provides experimental evidence that proton availability and the migration of potassium ions through the membrane are selectivity regulators that can lead to the formation of C_6 products from CO_2 reduction.

2. Results and discussion

As a starting point, LSV measurements were made in the presence of CO_2 and N_2-saturated acetonitrile and 0.1 M tetrabuty-lammonium hexafluorophosphate ($TBAPF_6$) for each studied anolyte and are presented in Fig. 1a. Pb electrodes show higher activity for the CO_2RR at a lower potential, with the higher pH anolyte exhibiting the start of the onset potential at -2.2 V ($vs.$ Ag/Ag$^+$), and no significant current density was observed for the

electrode under N_2-saturation. Moreover, at -2.5 V $vs.$ Ag/Ag$^+$, the alkaline anolyte (KOH 0.5 M) achieved three times higher current density than the near-neutral anolyte (KHCO$_3$ 0.5 M) and almost ten times the current density achieved for the acidic anolyte (H_2SO_4). Fig. 1b shows the stability of the Pb electrode with different electrolytes during CO_2 reduction. From chro-noamperometry curves collected during the reaction, it is possible to observe that the stability also depends on the anolyte type and pH. Over time, a current loss is observed in the acidic and near-neutral anolytes due to corrosion reactions at the electrode surface.

Moreover, higher current and stability are achieved using the alkaline anolyte (KOH) since K$^+$ ions, from the crossover, present near the Outer-Helmholtz plane, modulate the corrosion mech-anism by electrostatic repulsion of H$^+$, and it is associated with the carbon–carbon (C–C) coupling in the CO_2RR since elevated potassium ion concentrations also stabilized the intermedi-ates.[44,47] Although the potassium ion can promote the precipita-tion of the CO_2RR products and become a problem for some cell configurations,[48] in this case, it was used as a strategy to favour the C–C coupling to lead to higher-value products achieving competitive current density in non-aqueous media compared with the literature.[21,28,49] Electrochemical impedance spectroscopy spectra in Fig. 2a and b show that the reaction is accelerated with the availability of potassium ions in the anolyte. Low electron transfer resistance (see Table S2†) is observed in the following order: KOH < KHCO$_3$ < H_2SO_4. With the increase in the pH value and the minor proton availability, K$^+$ inhibits proton migration, and it is rapidly transported through the Nafion membrane to the catholyte solution,[50] increasing the potassium ion concentration and favouring the promotion of the C–C coupling.

Furthermore, the EIS for the Pb plate before (Fig. 2a) and after (Fig. 2b) the cyclic voltammetry cleaning shows a decrease in the electron transfer resistance after the complete cleaning process for the alkaline anolyte. For the other anolytes (H_2SO_4 and KHCO$_3$), an activity loss and a higher electron transfer resistance were observed, which can be associated with the intergranular corrosion (observed by SEM) that occurs right after the acidic cleaning and results in catalyst deactivation. The catalyst deactivation is also supported by the appearance of two charge-transfer resistances in series for KHCO$_3$ and H_2SO_4
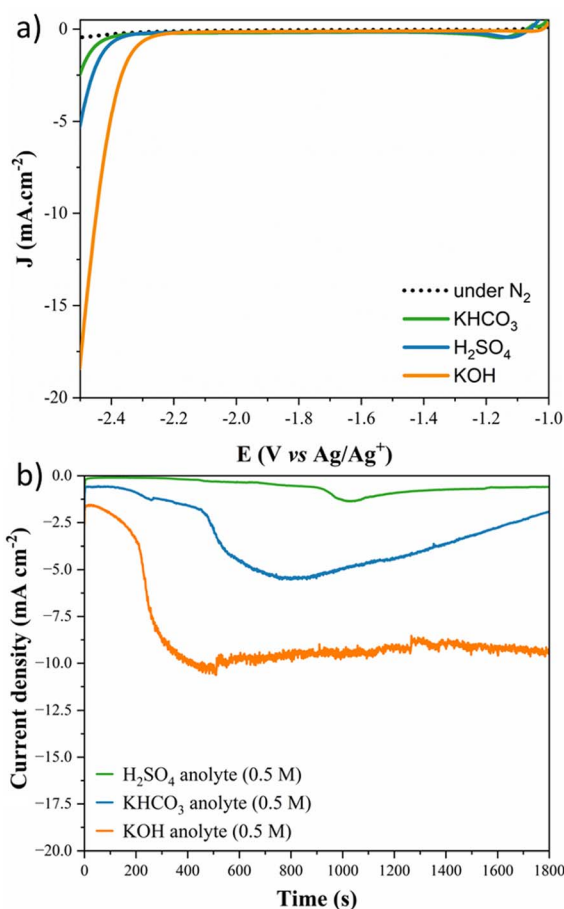

Fig. 1 (a) CO_2RR polarization curve for a Pb plate electrode in dried acetonitrile 0.1 M $TBAPF_6$ with H_2SO_4, KHCO$_3$, and KOH anolytes and (b) chronoamperometric curve for the different anolytes on the Pb plate.
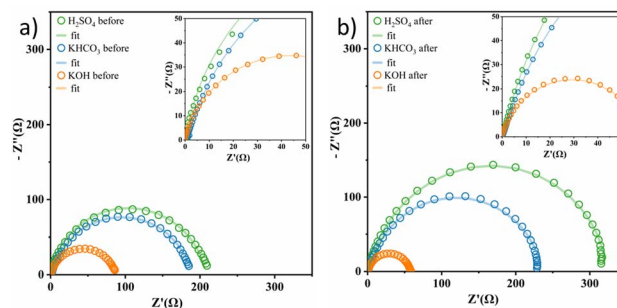

Fig. 2 Nyquist plots for the Pb plate under a CO_2 atmosphere for the different anolytes (a) before and (b) after the cyclic voltammetry cleaning step.

15830 | *J. Mater. Chem. A*, 2024, **12**, 15829–15836

This journal is © The Royal Society of Chemistry 2024

anolytes in the equivalent electrical circuit used for modelling the Pb electrode EIS, exhibited in Fig. S1.†

SEM images for each anolyte were obtained for the Pb electrode before and after the CO_2RR to evaluate the cathodic corrosion behaviour (Fig. 3). Due to the high reaction overpotential, cathodic corrosion is observed for all the anolytes' pH, but harsh deterioration is observed for acid and neutral anolytes. A higher H^+ concentration in the anolyte induces proton migration through the cation exchange membrane, leading to intergranular corrosion of the Pb plate with the reaction using the acidic and near-neutral anolyte, Fig. 3b and c, respectively. The electrode corrosion by intergranular corrosion causes activity loss for the CO_2RR over time, as seen in the current decay on the chronoamperometry graph (see Fig. 1b). The intergranular attack was not observed for the alkaline anolyte (Fig. 3d), though K^+ ions can promote the lead electrode's corrosion. Still, at higher magnification, restructuring of the flat Pb plate can be seen, similar to the Pb plate in the presence of a corrosion inhibitor.[51] The restructuring can also be related to the corrosion and electrodeposition processes of the lead ions.[52] The inductively coupled plasma-optical emission spectroscopy (ICP-OES) data presented in Table S1† showed that higher K^+ ions modify the corrosion process instead of inhibiting corrosion. In the presence of H^+ and low K^+ ions, cathodic corrosion occurs by the intergranular attack, which leads to activity loss. However, with a higher K^+ ion concentration, the anodic corrosion produces a porous structure that maintains high activity due to the metal etch pits formed on the surface. This phenomenon occurs due to the low stability of the dissolution intermediate in the non-protic medium,[53] which causes the partial conversion of the ions to their metallic state to form agglomerated particle spots,[54] as observed in the HRSEM images, Fig. 3. The formed porous structure can keep the catalyst's superficial active area even though a harsher metal dissolution chemical is used. These results suggest that the CO_2RR intermediates can adsorb on the electrode surface in higher K^+ ions due to the increase in surface porosity caused by the intense corrosion process and due to the potassium-stabilized effect of CO_2 intermediates at the catalyst surface, enabling their conversion to various products.[43,55] Even with the restructuring, only a minor current decay over time is seen, unlike the other anolyte pH that exhibits a significant current density decay over time. Post-reaction DRX analysis (Fig. 4) did not show the formation of different phases on the Pb plate surface even after the electrode corrosion for acid and near-neutral anolytes, showing no change in the bulk structure of the electrode.

The electrolysis using a K^+ source anolyte ($KHCO_3$ and KOH) produced a white precipitate due to cation migration through the Nafion membrane (Fig. 5), which was collected and washed in dry acetonitrile for analysis by FTIR and TGA. The FTIR spectrum (Fig. 6a) demonstrates that a mixture of compounds can be found in solid products. The CO_2 reduction products in non-aqueous media have a considerably simple mechanism, as revised in ref. 15, 16 and 18, and can be identified using the FTIR spectrum combined with an analytical separation method, such as HPLC. Fig. 6a shows bands that can be assigned to the tartrate and oxalate ions signalled on the spectrum with the black and red arrows, respectively. The band at ~3300 cm^{-1} can be assigned to the carboxylic acid in both compounds, and the band at 1585 cm^{-1} also confirms the presence of the products in the ion form due to the asymmetrical stretching of the carboxylate anions.[56] The bands that correspond to the COO–stretching and bending vibration can be assigned to the tartrate[56–58] (δCOO: 826 cm^{-1}; 707 cm^{-1}; and τCOO: 612 cm^{-1}) and oxalate[59–61] (νCOO: 1300 cm^{-1}, βCOO: 771 cm^{-1}, and WCOO: 520 cm^{-1}). Additionally, no presence of the supporting electrolyte in the solid products and no characteristic band (~1430 cm^{-1}) for potassium carbonate are observed.[62,63]

TGA/DTG analysis presented in Fig. 6b agrees with the FTIR spectrum. Three decomposition stages were verified from the TGA spectrum between 250 and 550 °C after water loss (>200 °C).[64] These three primary decomposition stages are associated with the mixed products obtained from the CO_2RR. The first and second stages (>350 °C) involve the decomposition of the tartrate ion into oxalate,[65] corresponding to $\sim20\%$ weight loss due to the detachment of gaseous CO_2 molecules from the
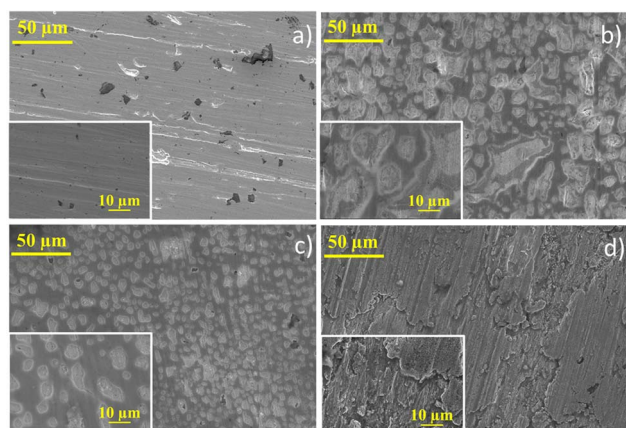

Fig. 3 Scanning electron microscopy images for (a) cleaned Pb plate before the reaction and for the Pb plate after the reaction using (b) acidic anolyte (H_2SO_4), (c) near-neutral anolyte ($KHCO_3$), and (d) alkaline anolyte (KOH).
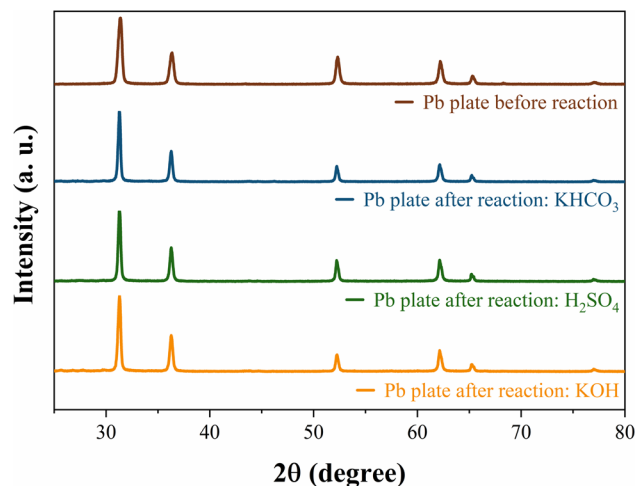

Fig. 4 XRD patterns of the Pb plate before and after CO_2 reduction in acetonitrile 0.1 M TBAPF$_6$ with different anolytes.
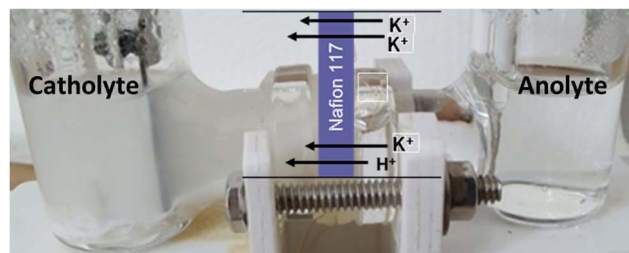
Fig. 5   H-cell picture showing the precipitate formation on the cath-olyte side after the CO_2RR in dry acetonitrile and KOH (0.5 M) as the anolyte.
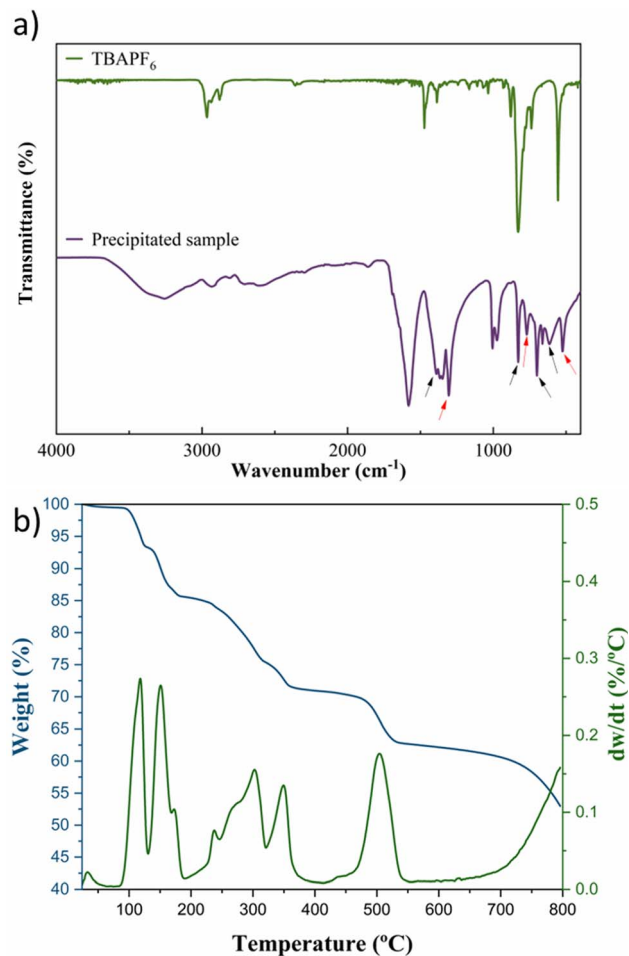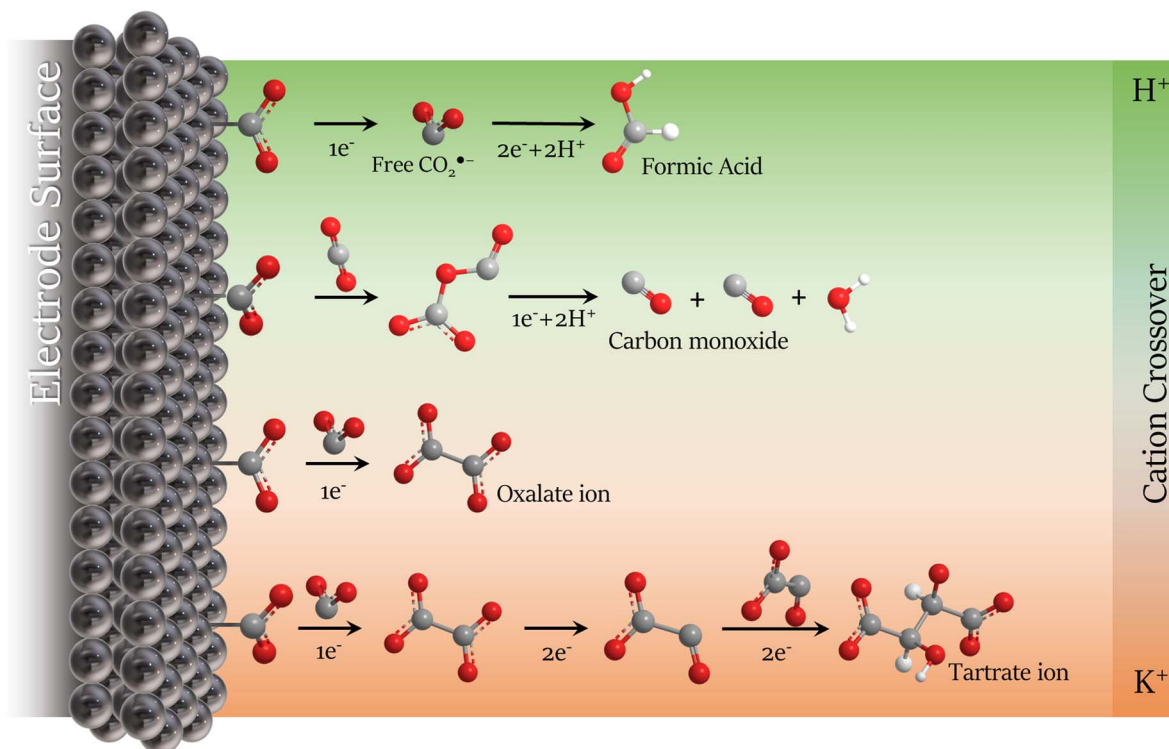
Fig. 6   (a) FTIR spectra for the precipitated CO_2RR products and the supporting electrolyte; (b) TG and DTG analysis for the precipitated products.

tartrate crystal lattice.[56] The third decomposition step involves the conversion of oxalate to carbonate with ~7% weight loss between 450 and 550 °C, corresponding to the CO evolution.[65,66] The mixture of the two solid products is due to the tartrate formation mechanism that occurs *via* the well-known process for converting CO_2 to oxalate/oxalic acid by coupling two $\cdot CO_2^-$ intermediates, followed by the dimerization of two oxalate molecules, summarized in Scheme 1 and described in Scheme 2a and b. With the main migration of H^+ (H_2SO_4 anolyte),

formic acid is the primary product of the CO_2RR.[67] However, with an increase in the K^+ migration, more C–C coupled products are obtained, as represented in Scheme 1, and the tartrate formation reaction is presented in Scheme 2.

The anolyte influence was verified by electrolysis at −2.3 V (*vs.* Ag/Ag$^+$) for each anolyte, and an HPLC with a UV detector was used to quantify the products. Since the mobile phase for the HPLC analysis was acidic water (pH = 3), the CO_2RR products were named by the protonated form. Also, it is essential to mention that experiments were carried out to evaluate the drying process in acetonitrile. In the collected post-reaction gas, only a trace of carbon monoxide from the CO_2RR was detected in the CG, without the formation of hydrogen at −2.5 V *vs.* Ag/Ag$^+$, showing the drying method's effectiveness. Fig. 7 exhibits the faradaic efficiency and the concentration of the detected products from the CO_2RR. When potassium-based salts are used in the anolyte, higher faradaic efficiency is seen for the C_{2+} products. Besides, the presence of the K^+ allows the formation of tartrate ions, which have been reported until now only by using an Ag-modified catalyst in the reduction reaction of glyoxylic acid[18] and not as a product of CO_2 reduction. To the best of our knowledge from the literature survey, Table S3,† this is reported for the first time for CO_2RR with a Pb catalyst. Published papers usually use acidic or non-aqueous anolytes, achieving higher selectivity and faradaic efficiency for oxalate/oxalic acid (>80%).[21,28,61,68] However, since the formation of tartrate depends on the viability of oxalate, the FE for carbonaceous products is expected to be lower. With the KHCO$_3$ anolyte, the FE achieved by analyzing the cathodic electrolyte was 28%, 10%, and 37% for oxalic (OA), formic (FA), and tartaric acid (TA), respectively. The remaining faradaic efficiency was attributed to carbon monoxide, the only product detected in the gas phase. Higher faradaic efficiency was found using the KOH anolyte, 31% for OA, 16% for FA, and 53% for TA. The anolyte pH influences the amount of C_{2+} products on the catholyte side, as seen in Fig. 7b. Higher pH anolytes and low proton availability favour potassium migration in the crossover competition between the H^+ and the K^+. With the minimum migration of the H^+, the reduction mechanism favours the C–C coupling,[16,18] decreasing the energy barrier for C_{2+} products caused by the influence of potassium ions on the microenvironment of the electrode surface.[34,43,69] These unprecedented results in non-aqueous electrolytes coincide with the recent reports for aqueous-based systems,[44–46] where K^+ ions can accelerate the carbon–carbon (C–C) coupling process, leading to more complex molecules from the CO_2 reduction (Scheme 1).

KOH was chosen as the anolyte to study the potential influence of CO_2 conversion to tartrate since it showed the highest FE value for this product. The evaluated potentials were selected by LSV. The potentials studied were the potential right at the beginning of the onset, where the increase in the current density is observed (−2.2 V *vs.* Ag/Ag$^+$), the potential at the end of the onset potential, where the current density growth is obvious (−2.3 V *vs.* Ag/Ag$^+$), and the potential after the onset (−2.5 V *vs.* Ag/Ag$^+$), see Fig. 1. Fig. 8a and b exhibit the faradaic efficiency and the concentration of the carbonaceous products at different potentials, respectively. In −2.2 V *vs.* Ag/Ag$^+$, the

15832 | *J. Mater. Chem. A*, 2024, **12**, 15829–15836

This journal is © The Royal Society of Chemistry 2024

Scheme 1 Schematic representation of CO_2RR mechanism modulation in non-aqueous electrolyte with the cation migration preference from the anolyte on the Pb plate surface in dried acetonitrile.
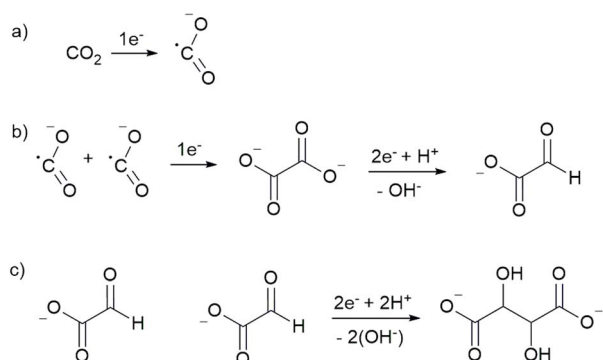
Scheme 2 The proposed tartrate mechanism formation is in high potassium ion availability media.

most favoured reaction with more than 50% of FE was the formation of formic acid, even with the K^+ ions. The amount of formic and oxalic acid produced was similar, but the rate of the tartaric acid was only 0.1 mM. At -2.5 V ($vs.$ Ag/Ag^+), more products were detected with a production rate of 0.17 μmol h^{-1} cm^{-2}, 0.13 μmol h^{-1} cm^{-2}, and 0.21 μmol h^{-1} cm^{-2} for oxalic,
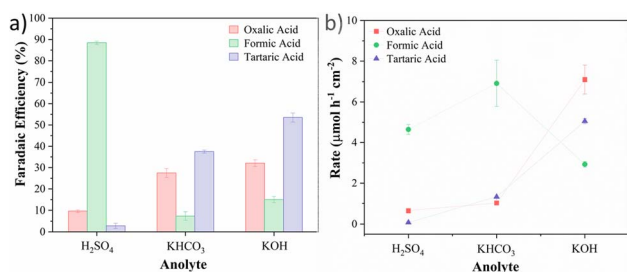

Fig. 7 Anolyte influence on the (a) faradaic efficiency for CO_2 reduction and on the (b) production rate for oxalic, formic, and tartaric acid at -2.2 V $vs.$ Ag/Ag^+.
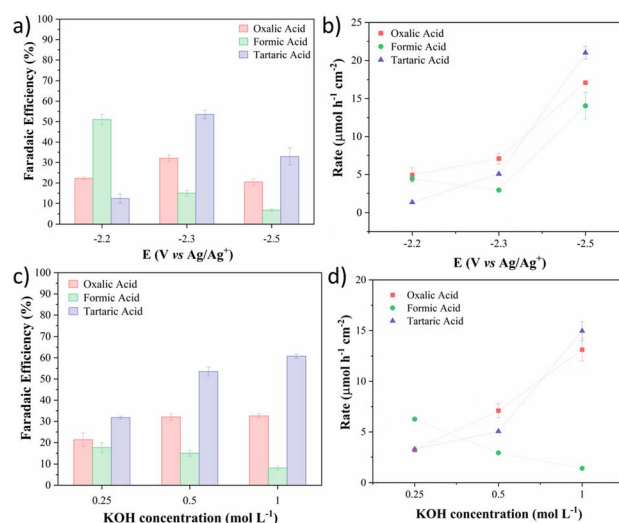

Fig. 8 (a) FE of electrochemical CO_2 reduction products and (b) production rate with applied potentials of -2.2, -2.3, and -2.5 V $vs.$ Ag/Ag^+ using KOH 0.1 M as the anolyte. (c) FE of CO_2 reduction products with different anolyte potassium ion concentrations and the (d) production rate for oxalic, formic, and tartaric acids.

Table 1 Parameters for the CO_2RR on acetonitrile (0.1 M TBAPF$_6$) and the faradaic efficiency and production rate of the organic acids

Acids	Anolyte (0.5M) at −2.3 vs. Ag/Ag$^+$			KOH 5 M: potential (vs. Ag/Ag$^+$)			KOH: anolyte concentration (M)		
	H$_2$SO$_4$	KHCO$_3$	KOH	−2.2	−2.3	−2.5	0.25	0.5	1.0
Faradaic efficiency (%)									
Formic	88.5	7.3	15.3	51.1	15.3	6.8	17.5	15.3	8.14
Oxalic	9.6	27.6	32	22.4	32	20.4	21.4	32	32.7
Tartaric	2.7	37.6	53.6	12.7	53.6	32.9	31.9	53.6	60.8
Production rate (μmol h^{-1} cm^{-2})									
Formic	4.69	6.94	2.97	4.33	2.97	14.05	6.37	2.97	1.46
Oxalic	0.71	1.04	7.10	4.97	7.10	17.10	3.32	7.10	13.16
Tartaric	0.06	1.33	5.01	1.32	5.01	21.00	3.17	5.01	14.95

formic, and tartaric acid respectively. A loss in faradaic efficiency is observed due to the rapid formation and consumption of the $\cdot CO_2^-$ intermediates that lead to the formation of gaseous CO (detected by GC). Fig. 8c and d show that when the anolyte concentration was improved, the electrolysis at the onset potential (−2.3 vs. Ag/Ag$^+$) produced a significant amount of the C$_{2+}$ products and a higher production rate was obtained (OA: 1.32 μmol h^{-1} cm^{-2} and TA: 1.49 μmol h^{-1} cm^{-2}) with good faradaic efficiency, 35% and 60% for OA and TA, respectively. Compared with the literature, this is the first time tartaric acid was produced from the CO_2RR using a Pb electrode in a non-aqueous medium (see Table S3†). Still, the tartaric acid formation achieved similar faradaic efficiency compared to recent reports.[21,23,28]

Unlike the potential increase, the increase in the K$^+$ concentration improved the production without losing energetic efficiency, emphasizing the potential of the potassium ion effect in non-aqueous media. All the studied parameters for the electrochemical CO_2 reduction using aqueous anolytes are summarized in Table 1.

3. Conclusions

In summary, we showed a route to produce tartaric acid from the CO_2RR in a non-aqueous medium by controlling the influence of the electrochemical configuration on modulating the faradaic efficiency and selectivity of the CO_2RR in non-aqueous media. We synthesized tartaric acid/tartrate from gaseous CO_2 using a commercial Pb plate as the cathode by modifying the anolyte to promote K$^+$ migration. The anolyte and supporting electrolytes were essential to achieve higher value-aggregated products from CO_2 waste. Tartaric acid production reached 60% faradaic efficiency with a higher KOH concentration at −2.3 V vs. Ag/Ag$^+$, producing 1.5 μmol L^{-1} in 30 minutes of electrolysis. This multi-carbon product formation is associated with the higher K$^+$ crossover, favouring the C–C coupling of the intermediates in the CO_2RR. In addition, the experimental results showed that the potassium ion has a more significant role in the coupling of intermediates than the increase in the reaction potential, and it is responsible for promoting the formation of C$_{4+}$ products from CO_2.

The present work provided an innovative and promising approach to convert CO_2 to multicarbon products, which are obtained in solid form (precipitated) and could be used strategically to design an easy and efficient separation process.

4. Experimental methods

4.1 Procedure for drying acetonitrile

Before the electrochemical experiments, the excess water in acetonitrile was removed using the methodology described by Williams and Lawton (2010).[70] A 3 A° molecular sieve is pre-dried at 300 °C for 24 h immediately before use. After drying, the molecular sieve is added to the acetonitrile (HPLC grade) at 10% m/v and left for 24 hours in a nitrogen atmosphere. The dried acetonitrile was kept in a sealed vial with molecular sieves and stored for one week after the drying procedure.

4.2 Ag/Ag$^+$ reference electrode preparation and calibration

The silver–silver ion reference electrode was prepared according to Izutsu (2013).[71] AgNO$_3$ salt was dissolved (0.01 M) in dry acetonitrile with the tetrabutylammonium hexafluorophosphate (TBAPF$_6$) supporting electrolyte (0.1 M). A cleaned silver wire was immersed in the freshly prepared solution using a glass shaft with a Teflon cap. The silver was cleaned by physical polishing with sandpaper and a chemical polishing step with 0.1 M HNO$_3$ solution.

The reference electrode was freshly prepared daily and calibrated using a ferrocene standard solution (5 mM ferrocene in 0.1 M TBAPF$_6$ in CH$_3$CN).

4.3 Electrochemical CO_2 reduction setup

The experiments were carried out in an H-type cell configuration with a cation exchange membrane (Nafion 117) using a Pb plate (1.5 × 1 cm^2), Pt mesh as working and counter electrodes, and an Ag/Ag$^+$ (0.01 M AgNO$_3$) reference electrode. The cell volume was 10 mL for the catholyte and 10 mL for the anolyte with magnetic stirring on the catholyte side. The catholyte used was 0.1 M TBAPF$_6$ in dried acetonitrile. Before each reaction, the electrolyte was pre-saturated with CO_2 for 30 minutes, and the investigated anolytes were H$_2$SO$_4$ (acid), KHCO$_3$ (near neutral), and KOH (alkaline) for the potential −2.2, −2.3, and −2.5 V vs. Ag/Ag$^+$.

The Pb plate was previously cleaned by polishing it with wet sandpaper (2000 grits), followed by electrochemical cleaning by

15834 | J. Mater. Chem. A, 2024, **12**, 15829–15836

This journal is © The Royal Society of Chemistry 2024

applying −1.8 V *vs.* Ag/AgCl (KCl 3 M) in an H_2SO_4 solution (0.1 M) for 500 seconds. Before each analysis, an additional cleaning step was made by cyclic voltammetry (−1 to −2.5 V *vs.* Ag/Ag^+) until current stabilization (around eight cycles), see Fig. S2.† All the electrochemical measurements were made using a potentiostat/galvanostat Autolab (model PGSTAT30, Metrohm).

4.4 Characterization

The Pb plates were characterized using a Shimadzu XRD-6000 diffractometer with Cu-Kα radiation ($\lambda = 1.5406$ Å) and a scanning rate of $2°$ min^{-1} from 10 to $80°$ at room temperature. The morphological characterization of the electrodes was performed using a scanning electron microscope (SEM-JSM6510). The electrochemical characterization was performed in a potentiostat/galvanostat Autolab with an FRA 32M module in an H-type cell with a Nafion 117 membrane and Ag/Ag^+ reference electrode and CO^2 pre-saturated acetonitrile (0.1 M TBAPF6) as the catholyte. Thermogravimetric analysis was carried out on a TGAQ500 (TA instruments) analyzer. The samples were heated in a platinum pan from 25 to 800 °C with a ramp rate of 10 °C min^{-1} under N_2 flux (40 mL min^{-1}). ICP-OES analysis was performed on the catholyte after each reaction. The acetonitrile on the electrolyte was dried overnight using a water bath (80 °C), and the solid was dissolved in a 4 M H_2SO_4 solution.

4.5 Product quantification

The total volume of the catholyte was collected, and the solid products were solubilized by adding water pH 3 (H_2SO_4) to the samples. The dilution was calculated for each experiment. The products were quantified using a high-performance liquid chromatography-HPLC (Shimadzu Prominence 20A liquid chromatograph LC-20AT equipped with a UV detector at 214 nm). An Agilent MetaCarb 87H (300 × 7.8 mm) column was used to separate the products at a temperature of 40 °C with an eluent flow rate of 0.6 mL min^{-1}, water pH 3.0 (H_2SO_4) as the mobile phase, and a sample injection volume of 20 μL. The total run time was 22.00 minutes, and the retention times were 6, 7.2, and 12.5 min for oxalic acid, tartaric acid, and formic acid, respectively (see Fig. S3–S6†). Gaseous products were collected by coupling a Tedlar® gas sample bag (1 L) in the electrochemical cell to collect the post-reaction gases along with the CO^2 flux. The collected gas was analyzed using argon as the carrier gas in a GC-Thermo gas chromatograph equipment with a carboxen 1010 plot capillary column.

Conflicts of interest

There are no conflicts to declare.

Acknowledgements

References

1 Y. Abdullatif, A. Sodiq, N. Mir, Y. Bicer, T. Al-Ansari, M. H. El-Naas and A. I. Amhamed, *RSC Adv.*, 2023, **13**, 5687–5722.

2 T. M. Gür, *Prog. Energy Combust. Sci.*, 2022, **89**, 100965.

3 S. Sun, Y. Wang, X. Zhao, C. Zhang and C. Wu, *Carbon Capture Sci. Technol.*, 2022, **5**, 100078.

4 S. Sun, Y. Zhang, C. Li, Y. Wang, C. Zhang, X. Zhao, H. Sun and C. Wu, *Sep. Purif. Technol.*, 2023, **308**, 122956.

5 P. Wienchol, A. Szlęk and M. Ditaranto, *Energy*, 2020, **198**, 117352.

6 L. Ou, S. Banerjee, H. Xu, A. M. Coleman, H. Cai, U. Lee, M. S. Wigmosta and T. R. Hawkins, *J. Cleaner Prod.*, 2021, **321**, 128779.

7 H. Choi, D.-K. Lee, M.-K. Han, G. Janani, S. Surendran, J. H. Kim, J. K. Kim, H. Cho and U. Sim, *J. Electrochem. Soc.*, 2020, **167**, 164503.

8 E. Ruiz-López, J. Gandara-Loe, F. Baena-Moreno, T. R. Reina and J. A. Odriozola, *Renewable Sustainable Energy Rev.*, 2022, **161**, 112329.

9 F. Proietto, A. Galia and O. Scialdone, *ChemElectroChem*, 2021, **8**, 2169–2179.

10 S. C. Jesudass, S. Surendran, G. Janani, T. H. Kim and U. Sim, *Adv. Energy Mater.*, 2023, **13**, 2301918.

11 Z. Huang, R. G. Grim, J. A. Schaidle and L. Tao, *Energy Environ. Sci.*, 2021, **14**, 3664–3678.

12 F. Franco, C. Rettenmaier, H. S. Jeon and B. Roldan Cuenya, *Chem. Soc. Rev.*, 2020, **49**, 6884–6946.

13 P. Saha, S. Amanullah and A. Dey, *Acc. Chem. Res.*, 2022, **55**, 134–144.

14 M. C. O. Monteiro, M. F. Philips, K. J. P. Schouten and M. T. M. Koper, *Nat. Commun.*, 2021, **12**(1), 1–7.

15 Y. I. Hori, Electrochemical CO_2 reduction on metal electrodes, *Modern aspects of electrochemistry*, 2008, pp. 89–189.

16 E. A. dos Reis, G. T. S. T. da Silva, E. I. Santiago and C. Ribeiro, *Energy Technol.*, 2023, **11**, 2201367.

17 J. Feng, S. Zeng, J. Feng, H. Dong and X. Zhang, *Chin. J. Chem.*, 2018, **36**, 961–970.

18 A. C. Garcia, C. Sánchez-Martínez, I. Bakker and E. Goetheer, *ACS Sustain. Chem. Eng.*, 2020, **8**, 10454–10460.

19 R. J. Gomes, C. Birch, M. M. Cencer, C. Li, S. B. Son, I. D. Bloom, R. S. Assary and C. V. Amanchukwu, *J. Phys. Chem. C*, 2022, **2022**, 13595–13606.

20 M. A. Murcia Valderrama, R. J. van Putten and G. J. M. Gruter, *Eur. Polym. J.*, 2019, **119**, 445–468.

21 V. Boor, J. E. B. M. Frijns, E. Perez-Gallent, E. Giling, A. T. Laitinen, E. L. V. Goetheer, L. J. P. van den Broeke, R. Kortlever, W. de Jong, O. A. Moultos, T. J. H. Vlugt and M. Ramdin, *Ind. Eng. Chem. Res.*, 2022, **61**(40), 14837–14846.

22 M. König, J. Vaes, E. Klemm and D. Pant, *iScience*, 2019, **19**, 135–160.

This journal is © The Royal Society of Chemistry 2024

J. Mater. Chem. A, 2024, **12**, 15829–15836 | **15835**

23 M. König, S. H. Lin, J. Vaes, D. Pant and E. Klemm, *Faraday Discuss.*, 2021, **230**, 360–374.

24 Y. Tomita and Y. Hori, *Stud. Surf. Sci. Catal.*, 1998, **114**, 581–584.

25 W. Lv, R. Zhang, P. Gao, C. Gong and L. Lei, *J. Solid State Electrochem.*, 2013, **17**, 2789–2794.

26 B. Eneau-Innocent, D. Pasquier, F. Ropital, J. M. Léger and K. B. Kokoh, *Appl. Catal., B*, 2010, **98**, 65–71.

27 E. Schuler, M. Demetriou, N. R. Shiju and G. J. M. Gruter, *ChemSusChem*, 2021, **14**, 3636–3664.

28 Y. Cheng, P. Hou, H. Pan, H. Shi and P. Kang, *Appl. Catal., B*, 2020, **272**, 118954.

29 B. J. Cook, G. N. Di Francesco, K. A. Abboud and L. J. Murray, *J. Am. Chem. Soc.*, 2018, **140**, 5696–5700.

30 A. Gennaro, A. A. Isse, M. G. Severin, E. Vianello, I. Bhugun and J. M. Savéant, *J. Chem. Soc., Faraday Trans.*, 1996, **92**, 3963–3968.

31 C. Amatore and J. M. Savéant, *J. Am. Chem. Soc.*, 1981, **103**, 5021–5023.

32 M. M. Cencer, C. Li, G. Agarwal, R. J. Gomes Neto, C. V Amanchukwu and R. S. Assary, *ACS Omega*, 2022, **11**, 43.

33 M. Marx, H. Frauendorf, A. Spannenberg, H. Neumann and M. Beller, *JACS Au*, 2022, **2**, 731–744.

34 M. Schreier, P. Kenis, F. Che and A. S. Hall, *ACS Energy Lett.*, 2023, **8**, 3935–3940.

35 S. C. Jesudass, S. Surendran, J. Y. Kim, T. Y. An, G. Janani, T. H. Kim, J. K. Kim and U. Sim, *Electrochem. Energy Rev.*, 2023, **6**, 27.

36 S. Bin Dolmanan, A. Böhme, Z. Fan, A. J. King, A. Q. Fenwick, A. D. Handoko, W. R. Leow, A. Z. Weber, X. Ma, E. Khoo, H. A. Atwater and Y. Lum, *J. Mater. Chem. A*, 2023, **11**, 13493–13501.

37 Z. Xing, L. Hu, D. S. Ripatti, X. Hu and X. Feng, *Nat. Commun.*, 2021, **12**(1), 1–11.

38 J. J. Lv, R. Yin, L. Zhou, J. Li, R. Kikas, T. Xu, Z. J. Wang, H. Jin, X. Wang and S. Wang, *Angew. Chem., Int. Ed.*, 2022, **61**, e202207252.

39 D. Wang, J. Mao, C. Zhang, J. Zhang, J. Li, Y. Zhang and Y. Zhu, *eScience*, 2023, **3**, 100119.

40 H. Wu, A. Singh-Morgan, K. Qi, Z. Zeng, V. Mougel and D. Voiry, *ACS Catal.*, 2023, **13**, 5375–5396.

41 T. C. Berto, L. Zhang, R. J. Hamers and J. F. Berry, *ACS Catal.*, 2015, **5**, 703–707.

42 M. Moura de Salles Pupo and R. Kortlever, *ChemPhysChem*, 2019, **20**, 2926–2935.

43 S. Chandrashekar, H. P. I. van Montfort, D. Bohra, G. Filonenko, H. Geerlings, T. Burdyny and W. A. Smith, *Nanoscale*, 2022, **14**, 14185–14190.

44 X. Zi, Y. Zhou, L. Zhu, Q. Chen, Y. Tan, X. Wang, M. Sayed, E. Pensa, R. A. Geioushy, K. Liu, J. Fu, E. Cortés and M. Liu, *Angew. Chem., Int. Ed.*, 2023, **62**, e202309351.

45 J. Yu, M. Sun, J. Wang, Y. Wang, Y. Li, P. Lu, Y. Ma, J. Zhou, W. Chen, X. Zhou, C.-S. Lee, B. Huang and Z. Fan, *Phys. Sci.*, 2023, **4**(4), 101366.

46 A. K. Surendran, G. L. Tripodi, E. Pluhařová, A. Y. Pereverzev, J. P. J. Bruekers, J. A. A. W. Elemans, E. J. Meijer and J. Roithová, *Natural Sciences*, 2023, **3**, e20220019.

47 G. A. El-Nagar, F. Haun, S. Gupta, S. Stojkovikj and M. T. Mayer, *Nat. Commun.*, 2023, **14**(1), 1–10.

48 M. Sassenburg, M. Kelly, S. Subramanian, W. A. Smith and T. Burdyny, *ACS Energy Lett.*, 2023, **8**, 321–331.

49 M. König, S. H. Lin, J. Vaes, D. Pant and E. Klemm, *Faraday Discuss.*, 2021, **230**, 360–374.

50 K. J. Chae, M. Choi, F. F. Ajayi, W. Park, I. S. Chang and I. S. Kim, *Energy Fuels*, 2008, **22**, 169–176.

51 H. M. A. El-Lateef, A. R. El-Sayed, H. S. Mohran and H. A. S. Shilkamy, *Int. J. Ind. Chem.*, 2019, **10**, 31–47.

52 T. J. P. Hersbach and M. T. M. Koper, *Curr. Opin. Electrochem.*, 2021, **26**, 100653.

53 T. Wirtanen, T. Prenzel, J. P. Tessonnier and S. R. Waldvogel, *Chem. Rev.*, 2021, **121**, 10241–10270.

54 A. I. Yanson, P. Rodriguez, N. Garcia-Araez, R. V. Mom, F. D. Tichelaar and M. T. M. Koper, *Angew. Chem., Int. Ed.*, 2011, **50**, 6346–6350.

55 J. E. Huang, F. Li, A. Ozden, A. S. Rasouli, F. P. G. de Arquer, S. Liu, S. Zhang, M. Luo, X. Wang, Y. Lum, Y. Xu, K. Bertens, R. K. Miao, C. T. Dinh, D. Sinton and E. H. Sargent, *Science*, 2021, **372**, 1074–1078.

56 T. S. Shyju, S. Anandhi and R. Gopalakrishnan, *CrystEngComm*, 2012, **14**, 1387–1396.

57 V. Mathivanan and M. Haris, *Spectrochim. Acta, Part A*, 2013, **102**, 341–349.

58 G. P. Srivastava, S. Mohan and Y. S. Jain, *J. Raman Spectrosc.*, 1982, **13**, 25–29.

59 V. S. Tomar, H. D. Bist and D. P. Khandelwal, *Appl. Spectrosc.*, 1970, **24**(6), 598–601.

60 M. C. Figueiredo, I. Ledezma-Yanez and M. T. M. Koper, *ACS Catal.*, 2016, **6**, 2382–2392.

61 S. Subramanian, K. R. Athira, M. A. Kulandainathan, S. S. Kumar and R. C. Barik, *J. CO2 Util.*, 2020, **36**, 105–115.

62 H. Du, C. T. Williams, A. D. Ebner and J. A. Ritter, *Chem. Mater.*, 2010, **22**, 3519–3526.

63 V. J. Bruckman and K. Wriessnig, *Environ. Chem. Lett.*, 2013, **11**, 65–70.

64 W. Liu, H. Wang, X. Gu, C. Quan and X. Dai, *Anal. Methods*, 2016, **8**, 2845–2851.

65 U. Tarpara, P. Vyas and M. J. Joshi, *Int. J. Nanosci.*, 2015, **14**(4), 1550013.

66 T. Yoshimori, Y. Asano, Y. Toriumi and T. Shiota, *Talanta*, 1978, **25**, 603–605.

67 J. Hussain, H. Jónsson and E. Skúlason, *ACS Catal.*, 2018, **8**, 5240–5249.

68 A. V. Rudnev, U. E. Zhumaev, A. Kuzume, S. Vesztergom, J. Furrer, P. Broekmann and T. Wandlowski, *Electrochim. Acta*, 2016, **189**, 38–44.

69 L. Gao, F. Bao, X. Tan, M. Li, Z. Shen, X. Chen, Z. Tang, W. Lai, Y. Lu, P. Huang, C. Ma, S. C. Smith, Z. Ye, Z. Hu and H. Huang, *Energy Environ. Sci.*, 2023, **16**, 285–294.

70 D. B. G. Williams and M. Lawton, *J. Org. Chem.*, 2010, **75**, 8351–8354.

71 K. Izutsu, Reference Electrodes for Use in Nonaqueous Solutions, in *Handbook of Reference Electrodes*, ed. G. Inzelt, A. Lewenstam and F. Scholz, Springer, Berlin, Heidelberg, 2013, DOI: 10.1007/978-3-642-36188-3_6.

15836 | *J. Mater. Chem. A*, 2024, **12**, 15829–15836

This journal is © The Royal Society of Chemistry 2024